



The First Mid-infrared Detection of HNC in the Interstellar Medium: Probing the Extreme Environment toward the Orion Hot Core

Sarah Nickerson^{1,2}, Naseem Rangwala¹, Sean W. J. Colgan¹, Curtis DeWitt³, Xinchuan Huang¹, Kinsuk Acharyya⁴, Maria Drozdovskaya⁵, Ryan C. Fortenberry⁶, Eric Herbst⁷, and Timothy J. Lee¹

¹ Space Science and Astrobiology Division, NASA Ames Research Center, Moffett Field, CA 94035 USA; sarah.nickerson@nasa.gov

² Bay Area Environmental Research Institute, Moffett Field, CA 94035, USA

³ USRA, SOFIA, NASA Ames Research Center MS 232-11, Moffett Field, CA 94035, USA

⁴ Physical Research Laboratory: Ahmedabad, Gujarat, India

⁵ Center for Space and Habitability, University of Bern, Gesellschaftsstrasse 6, CH-3012 Bern, Switzerland

⁶ Department of Chemistry and Biochemistry, University of Mississippi, MS 38655, USA

⁷ Departments of Chemistry and Astronomy, University of Virginia, McCormick Road, Charlottesville, VA 22904, USA

Received 2020 September 5; revised 2020 November 9; accepted 2020 November 11; published 2021 January 28

Abstract

We present the first mid-infrared (MIR) detections of HNC and H¹³CN in the interstellar medium, and numerous resolved HCN rovibrational transitions. Our observations span 12.8–22.9 μm toward the hot core Orion IRC2, obtained with the Echelon-Cross-Echelle Spectrograph aboard the Stratospheric Observatory for Infrared Astronomy (SOFIA). In particular, ~5 km s⁻¹ resolution distinguishes individual rovibrational transitions of the HNC and HCN P, Q, and R branches; and the H¹³CN R branch. This allows direct measurement of the species' excitation temperatures, column densities, and relative abundances. HNC and H¹³CN exhibit a local standard of rest velocity of -7 km s⁻¹ that may be associated with an outflow from nearby radio source I and an excitation temperature of about 100 K. We resolve two velocity components for HCN, the primary component also being at -7 km s⁻¹ with a temperature of 165 K. The hottest component, which had never before been observed, is at 1 km s⁻¹ with a temperature of 309 K. This is the closest component to the hot core's center measured to date. The derived ¹²C/¹³C = 13 ± 2 is below expectation for Orion's Galactocentric distance, but the derived HCN/HNC = 72 ± 7 is expected for this extreme environment. Compared to previous sub-millimeter and millimeter observations, our SOFIA line survey of this region shows that the resolved MIR molecular transitions are probing a distinct physical component and isolating the chemistry closest to the hot core.

Unified Astronomy Thesaurus concepts: [Infrared astronomy \(786\)](#); [Interstellar medium \(847\)](#); [Star formation \(1569\)](#); [Molecular spectroscopy \(2095\)](#); [Spectral line identification \(2073\)](#); [Molecular physics \(2058\)](#)

1. Introduction

The isomers hydrogen cyanide (HCN) and hydrogen isocyanide (HNC) have shown their ubiquity through a range of astrophysical phenomena since their first detection in Galactic star-forming regions (Snyder & Buhl 1971, 1972; Zuckerman et al. 1972; McGuire 2018). Galactic sources include comets in our solar system (Lis et al. 1997; Agúndez et al. 2014), Titan's atmosphere (Moreno et al. 2011), dark molecular clouds (Irvine & Schloerb 1984; Hirota et al. 1998), diffuse clouds (Turner et al. 1997; Liszt & Lucas 2001), star-forming regions (Tennekes et al. 2006; Loughnane et al. 2012), protoplanetary objects (Dutrey et al. 1997; Kastner et al. 1997; Herpin & Cernicharo 2000; Hrivnak et al. 2000; Graninger et al. 2015), circumstellar envelopes (Bujarrabal et al. 1994; Cernicharo et al. 1996, 2013), carbon stars (Harris et al. 2003), and the Galactic center's circumnuclear disk (Harada et al. 2015). The isotopes of HCN and HNC are useful for measuring nitrogen, carbon, and hydrogen isotopic ratios in star-forming regions and cores (Wampfler et al. 2014; Zeng et al. 2017; Colzi et al. 2018a, 2018b). They also play a role in grain-surface chemistry at low temperatures (Lo et al. 2015). HCN and HNC have also been detected in several external galaxies (Rickard et al. 1977; Henkel et al. 1988; Gao & Solomon 2004) including Seyfert galaxies (Pérez-Beaupuits et al. 2007), molecular outflows (Aalto et al. 2012), and high-redshift galaxies (Guélin et al. 2007).

Several studies have also discovered HCN or HNC in hot cores (Goldsmith et al. 1981; Schilke et al. 1992; Lahuis & van Dishoeck 2000; Boonman et al. 2001; Knez et al. 2001, 2009; Lacy et al. 2002; Rolffs et al. 2011). These warm (≥100 K), dense (10⁵–10⁸ cm⁻³) regions of the interstellar medium (ISM) near young, high-mass protostars. Stellar radiation heats the gas and dust grains, evaporates the icy dust mantles in the cold molecular cloud where the protostar formed, and reveals a chemically rich reservoir of complex organic molecules (Ohishi 1997; Kurtz et al. 2000; van der Tak 2004; Bisschop et al. 2007; Belloche et al. 2013; Rivilla et al. 2017). Hot cores are possibly the antecedents to later ultra-compact H II regions (Cesaroni 2005), representing a key stage in stellar evolution. Similar hot corinos envelop low-mass protostars (Bottinelli et al. 2004).

The HCN/HNC abundance ratio changes under different conditions in star-forming regions, providing a useful probe of regional properties. HCN/HNC nears unity at low temperatures (Irvine & Schloerb 1984; Schilke et al. 1992), infrared (IR) dark clouds (Vasyunina et al. 2011; Miettinen 2014) and dark cores (Hirota et al. 1998). Dark cores are defined as regions with temperatures ~10 K and densities of 10³–10⁵ cm⁻³ (Benson & Myers 1989). By comparison, in the Orion Molecular Cloud (OMC-1) region, the HCN abundance remains similar to these dark cores while the HNC abundance drops. HCN/HNC is ~80 toward the Orion hot core IRC2, and

drops to ~ 5 away from it (Schilke et al. 1992). Later observations in this region found a correlation between gas kinetic temperature and the HCN-to-HNC intensity ratio (Hacar et al. 2020).

These isomers are a promising chemical clock. Jin et al. (2015) measured the HCN/HNC abundance ratio in massive star-forming regions at differing evolutionary stages (IR dark clouds, high-mass protostellar objects, and ultra-compact H II regions), revealing that this ratio increases toward more advanced stages. Indeed, the evidence suggests that HNC is more prone to destruction at higher temperatures than HCN, and will be less abundant in more advanced protostellar objects as they heat the ISM.

Theoretical calculations predict the isomers' main formation pathway to be the dissociative recombination of HCNH^+ with an electron (Herbst 1978), and experiments find this produces near-equal quantities of HCN and HNC (Mendes et al. 2012). However, HNC is the less stable of the two isomers (Lee & Rendell 1991; Bowman et al. 1993; Nguyen et al. 2015) and should be even less abundant than observed (for an overview see Loison et al. 2014). Mechanisms proposed to regulate the HCN/HNC ratio include the gas-phase $\text{H} + \text{HNC}$ reaction barrier (Graninger et al. 2014), ultraviolet (UV) dissociation (Chenel et al. 2016; Aguado et al. 2017), and collisions with H_2 (Hernández Vera et al. 2017) and He (Sarrasin et al. 2010).

Despite being the first hot core discovered (Ho et al. 1979), Orion IRc2 is atypical. Most hot cores are mainly internally heated, enveloping their protostar, while IRc2 is heated externally without evidence of any internal source (Blake et al. 1996; Okumura et al. 2011). A previous explosive outflow may have heated it while it was a pre-existing dense clump, it may be itself an explosive outflow, or it is possibly a cavity offering a glimpse into a dust obscured protostar (Shuping et al. 2004; Goddi et al. 2011; Zapata et al. 2011; Bally et al. 2017; Orozco-Aguilera et al. 2017). The main candidate for IRc2's heat source is radio source I, a possible binary system of protostars (Hirota et al. 2017), which is heavily dust-obscured (Plambeck & Wright 2016) and considered to be the main energy source of the region (Hirota et al. 2015). Nonetheless IRc2's location in the Orion Molecular Cloud, the nearest massive star-forming region to Earth at 388 ± 5 pc (Kounkel et al. 2017), makes it ideal for observing the rich hot core chemistry.

Numerous HCN and HNC emission lines have been observed toward IRc2 in the millimeter (Goldsmith et al. 1986; Schilke et al. 1992) and sub-millimeter (Stutzki et al. 1988; Harris et al. 1995; Schilke et al. 2001; Comito et al. 2005), two well-studied spectral regions due to their accessibility from the ground. However, observations in the mid-IR (MIR) have been scarce due to atmospheric absorption. The MIR is nonetheless critical for understanding fully the chemistry of the ISM. Additionally, rovibrational transitions for molecules with no permanent dipole moment are accessible only in the this wavelength range.

The Short-Wavelength Spectrometer aboard the Infrared Space Observatory covered $2.38\text{--}45.2 \mu\text{m}$ (de Graauw et al. 1996), but detection was limited to the strongest absorption features and not individual rovibrational transitions in hot cores (van Dishoeck et al. 1998; Lahuis & van Dishoeck 2000; Boonman et al. 2003). Similarly, Spitzer's Infrared Spectrograph (Houck et al. 2004) could only detect the strongest HCN absorption feature toward young stellar objects (Lahuis et al. 2006; An et al. 2009, 2011).

The ground-based Texas Echelon-Cross-Echelle Spectrograph (TEXES; Lacy et al. 2002) resolves these individual transitions from 5 to $25 \mu\text{m}$ with a maximum resolving power of $\sim 100,000$, but TEXES cannot access the entire MIR range due to atmospheric interference. HCN rovibrational and rotational transitions were detected with TEXES toward the hot cores AFGL 2591 (Knez et al. 2001), NGC 7538 IRS 1 (Knez et al. 2009), and IRc2 (Lacy et al. 2002, 2005).

The Stratospheric Observatory for Infrared Astronomy (SOFIA; Young et al. 2012) is an airborne observatory that flies above 99% of atmospheric water vapor. The Echelon-Cross-Echelle Spectrograph instrument (EXES; Richter et al. 2018) aboard SOFIA observes in the MIR from 5 to $28 \mu\text{m}$ with a spectral resolution of $10^3\text{--}10^5$. Currently, this is the only spectrograph able to resolve individual molecular transitions over the entire MIR. Several studies of hot cores with SOFIA/EXES are ongoing (Indriolo et al. 2015a, 2020; Barr et al. 2018, 2020; Dungee et al. 2018). Rangwala et al. (2018) detected eight HCN R-branch rovibrational transitions toward IRc2 between 12.96 and $13.33 \mu\text{m}$, enough to directly calculate its temperature and column density.

In this work, we present high-resolution observations of HCN, H^{13}CN , and HNC toward the hot core Orion IRc2 from 12.8 to $22.9 \mu\text{m}$. This is the first ISM detection of HNC and H^{13}CN in the MIR. Additionally, at MIR wavelengths, SOFIA's beam size ($3''.2 \times 3''.2$) is much smaller compared with space-based missions like ISO ($14'' \times 27''$) and most previous sub-millimeter/millimeter studies from the ground. This enables us to unambiguously isolate a previously unprobed, hotter component of molecular gas, traced by HCN, closest to the hot core from the surrounding emission.

We provide our observational methods in Section 2, detail our analysis in Section 3, discuss the implications of the results and compare them with both other observations and models in Section 4, and summarize our conclusions in Section 5. Our observations are part of a wider molecular survey of Orion IRc2 in the MIR from 7.2 to 8 and 13.2 to $28.3 \mu\text{m}$ (publication in preparation).

2. Observations and Data Reduction

We observed Orion IRc2 with the EXES instrument aboard the SOFIA observatory between 2018 October 27 and 31 at altitudes from about 42,000 to 44,000 ft in high-low mode. Spectra were acquired in the cross-dispersed high-resolution mode with a slit width of $3''.2$ giving a resolving power of about 60,000 ($\sim 5 \text{ km s}^{-1}$). We used the cross-disperser grating in first order to obtain the broadest simultaneous wavelength coverage per spectral setting. The length of the slit varied between $1''.9$ and $6''.9$, depending on the spectral setting. Table 1 gives the details for these six settings, each of which is split into several orders. For all observations, we nodded the telescope to an off-source position relatively free of emission $15''$ east and $25''.9$ north of IRc2, at 1 minute intervals, in order to remove sky emission and thermal background from the telescope system.

We reduce the EXES data with the SOFIA Redux pipeline (Clarke et al. 2015). Wavelength scales are calibrated using sky emission line spectra produced for each setting by omitting the nod subtraction step and then adjusting the scale to match observed sky emission line wavelengths to their values in the HITRAN database (Gordon et al. 2017). The absolute velocity uncertainty is $0.15\text{--}0.3 \text{ km s}^{-1}$, estimated from high-medium

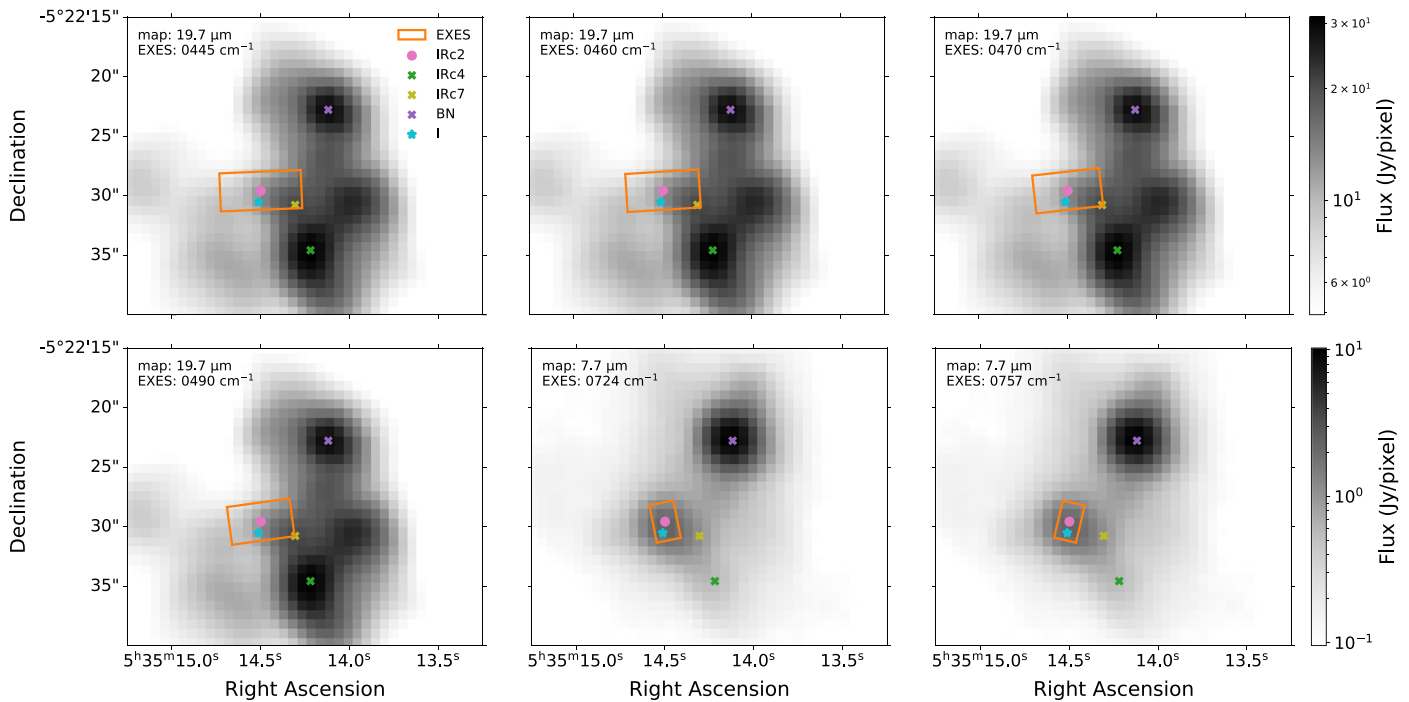


Figure 1. Echelon-Cross-Echelle Spectrograph (EXES) footprint for each setting superimposed on a SOFIA/FORECAST map of the region (de Buizer et al. 2012). In addition to our target, IRc2, the positions of radio source I and nearby IR sources IRc4, IRc7, and BN are given. Note that, in order to display maps closest in wavelength to each EXES setting, the $7.7 \mu\text{m}$ map is for the 700 cm^{-1} setting, and the $19.7 \mu\text{m}$ map is for the 400 cm^{-1} setting. Their flux scales differ, given by the grayscale bars on the right.

Table 1
Specifications for Each EXES Setting

Setting (cm^{-1})	Species	Min λ (μm)	Max λ (μm)	Date (yyyy-mm-dd)	Altitude (ft)	Slit Length \times Width ($'' \times ''$)	Integration Time (s)
757	HCN	12.8	13.6	2018-10-31	42,008	1.9×3.2	2560
724	HCN, H^{13}CN	13.5	14.3	2018-10-30	44,002	2.1×3.2	2880
490	HNC	20.1	20.8	2018-10-27	43,014	5.3×3.2	576
470	HNC	20.8	21.5	2018-10-27	43,015	5.7×3.2	512
460	HNC	21.5	22.2	2018-10-27	42,010	6.2×3.2	512
445	HNC	22.2	22.9	2018-10-27	42,005	6.9×3.2	512

mode sky lines of other settings. Figure 1 gives the EXES footprint for each observational setting over SOFIA/FORECAST maps at 7.7 and $19.7 \mu\text{m}$ (de Buizer et al. 2012). Each observation is centered over IRc2, and we also show the positions of IR sources IRc4, IRc7, and BN, and radio source I, which has no IR component and may be heating IRc2. For settings 445 and 460 cm^{-1} , in particular, we were concerned about contamination and dilution from IRc7. However, after examining spectra split along the slit width, we confirm that the spectral lines originate from the slit center, over IRc2, and not the edge over IRc7. Furthermore, from ground-based MIR spectroscopy of IRc2 and IRc7, Evans et al. (1991) found that C_2H_2 and HCN have two and three times higher column densities, respectively, toward IRc2 than IRc7. Therefore, our observations are centered over IRc2 and are unlikely to be contaminated by IRc7.

We find HCN in two settings covering $701\text{--}783 \text{ cm}^{-1}$ ($12.8\text{--}14.3 \mu\text{m}$), H^{13}CN in one setting from 701 to 725 cm^{-1} ($13.5\text{--}14.3 \mu\text{m}$), and HNC in four settings from 436 to 498 cm^{-1} ($20.1\text{--}22.9 \mu\text{m}$). We searched for, but did not observe, the isotopologues HC^{15}N and DCN with the HITRAN (Gordon et al. 2017) and GEISA (Jacquinet-Husson et al. 2016)

databases respectively and HN^{13}C and H^{15}NC with our own theoretically calculated line lists. Figure 2 shows an example of spectra for the 724 and 460 cm^{-1} settings with lines of HCN, H^{13}CN , and HNC.

3. Analysis

3.1. Peak Finding

In order to normalize our fluxes we must first identify the peaks and the baseline of each order. We employ a simple peak-finding algorithm to identify minima and maxima. For a given order, we perform Gaussian smoothing on the flux and then take the sign of the derivative of the smoothed flux. We consider blocks of consecutive pixels with the same sign. If two blocks of opposite signs are adjacent, or have a small gap between them, they are considered to belong to a peak and the peak position is taken to be the center of the gap between them. If a block is next to an order endpoint, then that endpoint is considered a peak. Three input parameters to the peak-finder, on occasion, require adjustment depending on the order: sigma for strength of Gaussian smoothing, number of consecutive

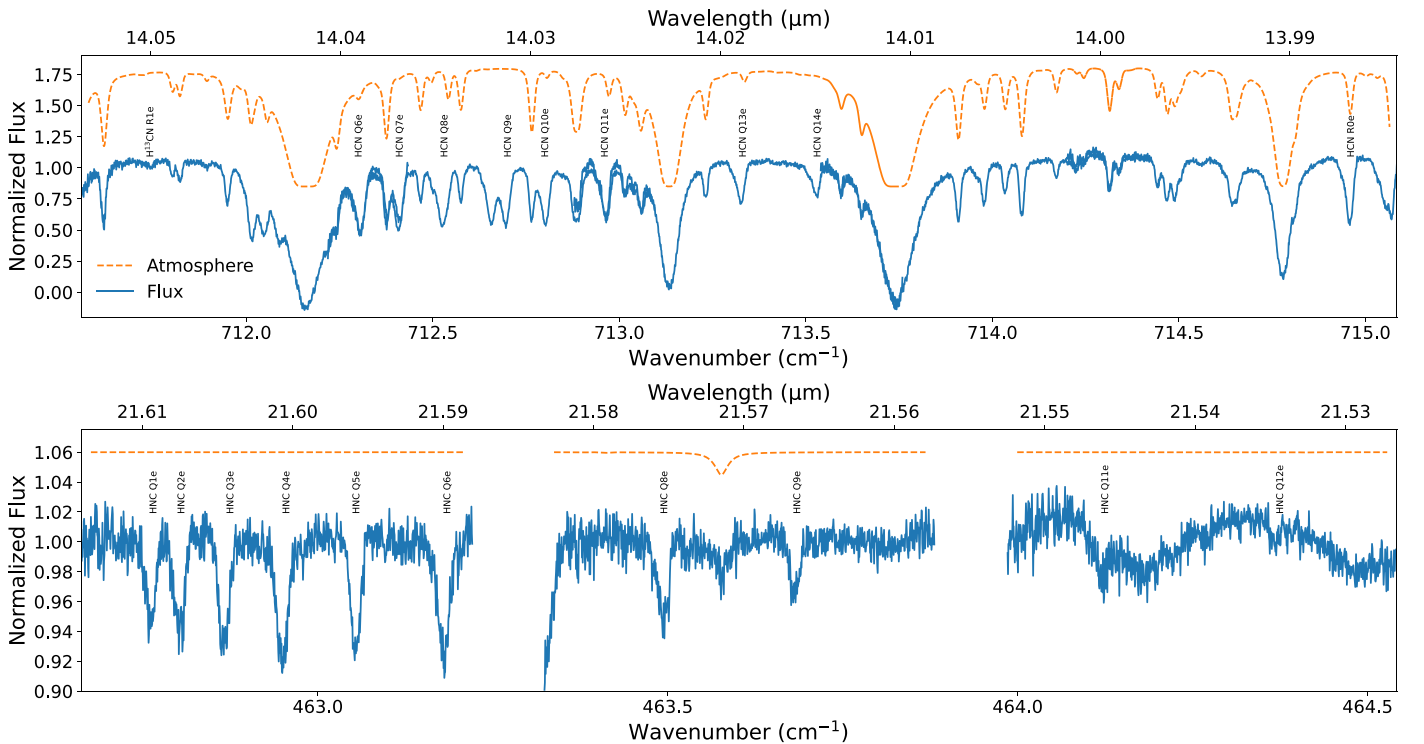


Figure 2. Sample of EXES spectra for HCN (top), H^{13}CN (top), and HNC (bottom). The flux is normalized and the atmosphere smoothed according to Section 3.2 and offset for display purposes. Note that, in the top panel, lines overlap from adjacent orders. The bottom panel shows three separated orders, the leftmost two of which have been baseline corrected by a polynomial, while the rightmost has not due to the absence of a satisfactory polynomial.

pixels with the same sign to be considered a block, and the size of the gap between blocks of consecutive pixels.

3.2. Normalization and Atmospheric Line Correction

While the lines in settings 445, 460, 470, and 490 cm^{-1} are clear of atmospheric features, many lines in 724 and 757 cm^{-1} are mixed with atmospheric lines, necessitating correction (for example: HCN Q8e, top panel of Figure 2). We download the unsmoothed ATRAN atmospheric model (Lord 1992)⁸ for each setting given their altitude, latitude, and zenith of observation. This unsmoothed ATRAN model corresponds to infinite resolution. To divide the ATRAN from our flux, we seek to smooth ATRAN to EXES’s resolution and normalize our flux to ATRAN simultaneously.

Each order requires a different normalization, especially the settings $445\text{--}490\text{ cm}^{-1}$ while an entire setting should have the same resolution. To achieve this, we implement the following procedure on the fluxes from each order.

1. For each individual order, we run the peak finder described in Section 3.1 on the observed EXES flux and the ATRAN model.
2. Due to standing waves in settings 445 and 460 cm^{-1} , a few orders require baseline correction where possible (see Figure 2, bottom panel). Considering all pixels not in a peak to be part of the baseline, we fit the baselines of these orders to a polynomial, n_b , and divide the flux by this polynomial in order to straighten the baseline.
3. We mask peaks that appear in the EXES flux and not in the ATRAN model, as well as deep CO_2 lines that

bottomed out at 0 in ATRAN but extended to negative in EXES (see Figure 2, top panel, for three examples). This leaves us with fluxes F_A from ATRAN and F_E from EXES that match.

4. We conduct the following procedure on each order:

$$\min \left[\sum_i^{\text{pixels}} \left\| \text{G1d}[F_{A,i}, \sigma_G] - \frac{F_{E,i}}{n_{b,i}n_c} \right\| \right], \quad (1)$$

where $F_{A,i}$ is the ATRAN model flux at pixel i , $F_{E,i}$ is the our observed EXES flux at pixel i , $n_{b,i}$ is the normalization polynomial’s value at pixel i if needed (otherwise $n_{b,i} = 1$, see step 2 above), n_c is the normalization constant, \min is the routine `optimize.minimize` from the `scipy` python package (Virtanen et al. 2020) that minimizes its enclosed function, and `G1d` is the routine `scipy.ndimage.Gaussian_filter1d` that smooths its enclosed function with standard deviation σ_G . $F_{A,i}$, $F_{E,i}$, and $n_{b,i}$ are inputs to Equation (1), and \min returns the values of n_c and σ_G that minimize Equation (1). We are finding the resolution and flux normalization that minimizes the difference between the ATRAN model and our observed EXES flux.

5. We retain n_c for each individual order, but discard σ_G , because many orders do not have enough, or any, ATRAN lines to match accurately the resolution. With each order normalized individually, we input the fluxes from an entire setting back into Equation (1) to obtain that setting’s overall σ_G .
6. We divide the order-normalized EXES flux by the setting-wide smoothed ATRAN model to correct for the atmosphere and use this flux for line fitting in Section 3.3.

⁸ <https://atran.arc.nasa.gov/cgi-bin/atran/atran.cgi>

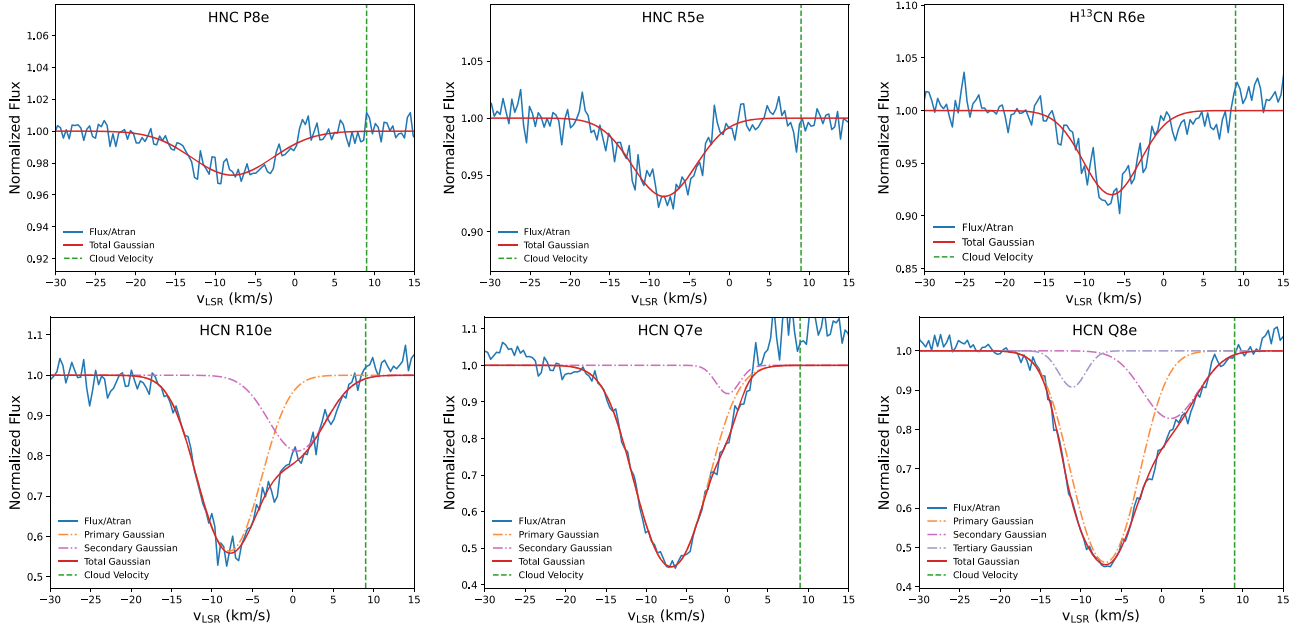


Figure 3. Gaussian fits for selected HNC (top left two), H^{13}CN (top right), and HCN (bottom row) lines normalized to their baselines. The HCN and H^{13}CN fluxes have been corrected for atmospheric absorption. HNC and H^{13}CN are best fit by a single Gaussian, while HCN is best fit by a double Gaussian showing two velocity components. For the case of Q8e, two Gaussians are needed for the main velocity component to catch distortion from atmospheric division. The main velocity component of HCN is similar to that of HNC and H^{13}CN . The vertical dotted line indicates the systematic, ambient cloud velocity of 9 km s^{-1} (Zapata et al. 2012).

3.3. Line Fitting

We rerun the peak finder from Section 3.1 on the normalized flux to match these peaks with the molecular absorption lines of interest. In many cases, this is sufficient to correctly identify the lines' extent. We only need to manually identify line boundaries in cases where the line was either weak or one of many in a crowded region. For settings 724 and 757 cm^{-1} , we also correct for atmosphere as in Section 3.2, while this is unnecessary for the other settings as no lines are near to any atmospheric absorption.

With `scipy.optimize.curvefit`, we fit the measured absorption lines with a Gaussian profile following Indriolo et al. (2015b):

$$I = I_0 e^{-\tau_0 G}, \quad (2)$$

where

$$G = \exp\left[-\frac{(v - v_c)^2}{2\sigma_v^2}\right], \quad (3)$$

I_0 is the normalized continuum level (typically close to unity), τ_0 is the line center optical depth, v is the local standard of rest (LSR) velocity, v_c is the velocity of the line center, and σ_v is the velocity dispersion. In the cases of double Gaussians, 1 and 2, we fit

$$I = I_0 e^{-(\tau_{01}G_1 + \tau_{02}G_2)}. \quad (4)$$

Triple Gaussians follow a similar equation. Each HNC and H^{13}CN line is best fit by a single Gaussian. Almost all HCN lines show two velocity components and are best fit by a double Gaussian with a handful of exceptions. P3e, R17e, and R18e are not resolved enough for a double Gaussian. Q9e and R12e overlap with acetylene absorption lines, leaving single Gaussians. Q8e, Q11e, Q14e, and R6e overlap with atmospheric lines that are divided out. However, due to the ATRAN

model not matching the data exactly, the remaining flux is slightly distorted and a triple Gaussian fits these lines best to correct for this distortion.

Figure 3 shows six examples of fits, with single Gaussians for HNC and H^{13}CN , and double or triple Gaussians for HCN. HCN R10e is an example of where the secondary velocity component is distinct. While HCN Q7e is similarly best fit by a double Gaussian, an atmospheric line falls over the secondary component and little remains after atmospheric correction. In cases such as this, we consider the entire line as belonging to the primary velocity component, even though some trace of the secondary remains. Q8e is an example of a triple Gaussian, where even after atmospheric correction the primary Gaussian is distorted and two Gaussians fit it best. Another Gaussian fits the secondary velocity component.

We calculate the column density, N_l , in the lower state of an observed transition from the integral over the absorption line:

$$\begin{aligned} dN_l/dv &= \frac{g_l}{g_u} \frac{8\pi}{A\lambda^3} \tau_0 G, \\ N_l &= \sqrt{2\pi} \frac{g_l}{g_u} \frac{8\pi}{A\lambda^3} \tau_0 \sigma_v, \end{aligned} \quad (5)$$

where g_l and g_u are the lower and upper statistical weights respectively, A is the Einstein constant for spontaneous emission, and λ is the rest wavelength of the transition. We obtain these parameter values (along with E_l required in Section 3.4) for HCN and H^{13}CN from the HITRAN database (Gordon et al. 2017) and for HNC from the GEISA database (Jacquinet-Husson et al. 2016).

Tables 2–4 list the best-fit parameters with fitted errors as well as the relevant molecular database parameters for HNC, H^{13}CN , and HCN respectively. All three species transition from the ground state to the ν_2 band. A number of lines are missing

Table 2
Observed ν_2 Band HNC Transitions and Inferred Parameters

Transition	Wavenumber (cm^{-1})	E_l/k_B (K)	g_l	A (s^{-1})	v_{LSR} (km s^{-1})	v_{FWHM} (km s^{-1})	τ_0	N_l $\times 10^{14} \text{cm}^{-2}$
P3e	453.64798	26.1	42	1.269	-6.8 ± 0.3	12.6 ± 1.5	0.031 ± 0.003	1.09 ± 0.20
P5e	447.5964	65.3	66	1.352	-7.0 ± 0.2	10.6 ± 0.5	0.041 ± 0.001	0.94 ± 0.05
P6e	444.57022	91.4	78	1.353	-5.3 ± 0.4	14.4 ± 2.0	0.029 ± 0.003	0.86 ± 0.19
P7e	441.54388	121.8	90	1.345	-9.1 ± 0.3	10.5 ± 1.3	0.031 ± 0.003	0.65 ± 0.11
P8e	438.51747	156.6	102	1.33	-7.9 ± 0.3	11.8 ± 1.1	0.028 ± 0.002	0.64 ± 0.08
Q1e	462.74319	4.4	18	3.379	-8.9 ± 0.2	10.3 ± 0.7	0.057 ± 0.003	0.46 ± 0.04
Q2e	462.78519	13.1	30	3.379	-8.1 ± 0.2	12.8 ± 1.2	0.071 ± 0.004	0.71 ± 0.10
Q3e	462.84818	26.1	42	3.38	-8.9 ± 0.1	11.7 ± 0.6	0.080 ± 0.003	0.73 ± 0.06
Q4e	462.93214	43.5	54	3.382	-8.4 ± 0.2	11.6 ± 0.6	0.080 ± 0.003	0.72 ± 0.05
Q5e	463.03705	65.3	66	3.383	-8.3 ± 0.1	10.7 ± 0.4	0.082 ± 0.002	0.69 ± 0.04
Q6e	463.16287	91.4	78	3.385	-8.4 ± 0.2	13.2 ± 0.5	0.078 ± 0.003	0.81 ± 0.04
Q8e	463.47714	156.6	102	3.39	-7.7 ± 0.2	12.6 ± 1.0	0.055 ± 0.003	0.54 ± 0.06
Q9e	463.66551	195.8	114	3.393	-7.7 ± 0.3	10.5 ± 1.0	0.037 ± 0.002	0.30 ± 0.04
Q11e	464.10446	287.1	138	3.4	-8.1 ± 0.5	7.7 ± 2.5	0.022 ± 0.005	0.13 ± 0.07
Q12e	464.35494	339.3	150	3.404	-5.9 ± 0.6	8.6 ± 1.6	0.013 ± 0.002	0.09 ± 0.02
R0e	465.74576	0.0	6	2.298	-8.3 ± 0.3	11.9 ± 1.3	0.037 ± 0.003	0.17 ± 0.03
R1e	468.76863	4.4	18	2.113	-8.0 ± 0.2	14.6 ± 0.7	0.069 ± 0.003	0.79 ± 0.05
R2e	471.7907	13.1	30	2.053	-8.1 ± 0.2	12.3 ± 0.8	0.076 ± 0.003	0.92 ± 0.08
R3e	474.8119	26.1	42	2.037	-8.0 ± 0.2	11.3 ± 0.6	0.081 ± 0.003	1.01 ± 0.08
R5e	480.85136	65.3	66	2.055	-8.2 ± 0.2	9.3 ± 0.5	0.071 ± 0.003	0.81 ± 0.04
R7e	486.88636	121.8	90	2.102	-7.7 ± 0.3	12.4 ± 1.0	0.048 ± 0.003	0.78 ± 0.07
R8e	489.902	156.6	102	2.131	-6.2 ± 0.3	9.2 ± 1.0	0.042 ± 0.003	0.51 ± 0.08
R9e	492.91629	195.8	114	2.163	-7.8 ± 0.3	12.9 ± 0.9	0.043 ± 0.002	0.75 ± 0.06
R10e	495.92916	239.3	126	2.197	-5.9 ± 0.5	8.4 ± 1.3	0.026 ± 0.004	0.30 ± 0.07

Note. Wavenumber is the rest wavenumber of the transition, E_l is the energy level of the lower state, k_B is the Boltzmann constant, g_l is the lower statistical weight, A is the Einstein constant, v_{LSR} is the observed local standard of rest velocity, v_{FWHM} is the observed full-width half-maximum, τ_0 is the observed optical depth, and N_l is the observed column density of the transition. Data in the first five columns are from the GEISA database (Jacquinet-Husson et al. 2016).

Table 3
Observed ν_2 Band H^{13}CN Transitions and Inferred Parameters

Transition	Wavenumber (cm^{-1})	E_l/k_B (K)	g_l	A (s^{-1})	v_{LSR} (km s^{-1})	v_{FWHM} (km s^{-1})	τ_0	N_l $\times 10^{14} \text{cm}^{-2}$
R1e	711.72312	4.1	36	1.206	-7.5 ± 0.4	8.7 ± 0.9	0.059 ± 0.005	2.46 ± 0.27
R6e	726.098321	87.0	156	1.143	-6.5 ± 0.2	8.2 ± 0.6	0.083 ± 0.005	5.30 ± 0.44
R8e	731.839651	149.2	204	1.157	-5.7 ± 0.3	7.0 ± 0.8	0.054 ± 0.005	3.05 ± 0.40

Note. See Table 2 for column descriptions. Data in the first five columns are from the HITRAN database (Gordon et al. 2017).

due to gaps between orders or heavy interference from atmospheric and acetylene lines.

In the case of HCN, a superscript on the column density indicates to which velocity component the Gaussian fit belongs. These components separately contribute to rotation diagrams in Section 3.4. For components with more than one Gaussian fit, the column density is the total of the Gaussian fits comprising it, while the velocity will be the velocity of the component with the highest optical depth. This is because the shallower components are artifacts of atmospheric lines.

The LSR velocities of HNC, H^{13}CN , and the primary component of HCN fall in the range of ~ -6 to -8 km s^{-1} , making it highly likely that they trace the same component in IRc2. The secondary HCN velocity component is $\sim 1 \text{ km s}^{-1}$. The line widths ($v_{\text{FWHM}} = 2\sqrt{2 \ln 2} \sigma_v$) of HNC are systematically higher than the primary component of HCN by about 3 km s^{-1} . Furthermore, Rangwala et al. (2018), observing the same HCN transitions as the present work, only resolve a single HCN velocity component with v_{FWHM} between 9 and 14 km s^{-1} , which is comparable to the HNC line widths in

Table 2. Clearly, HNC may also have an unresolved, secondary velocity component. HNC would be more highly depleted in this hotter component, making it more difficult for EXES to detect.

Two HCN lines, R17e and R18e, are not counted toward any component, due to high noise and LSR velocities of $\sim -1 \text{ km s}^{-1}$, which do not fit with either component. These lines were not resolved enough for a fit consistent with the other lines, but we include their derived parameters nonetheless in Table 4 for completeness as they are clearly detected in Rangwala et al. (2018).

3.4. Rotation Diagrams

For molecular populations in local thermal equilibrium (LTE), the level populations follow a Boltzmann distribution (Goldsmith & Langer 1999) given by

$$\ln \frac{N_l}{g_l} = \ln \frac{N}{Q_R(T_{\text{ex}})} - \frac{E_l}{k_B T_{\text{ex}}} \quad (6)$$

Table 4
Observed ν_2 band HCN Transitions and Inferred Parameters

Transition	Wavenumber (cm^{-1})	E_l/k_B (K)	g_l	A (s^{-1})	v_{LSR} (km s^{-1})	v_{FWHM} (km s^{-1})	τ_0	N_l $\times 10^{14} \text{cm}^{-2}$
P2e	706.0664	12.8	30	0.6576	-7.5 ± 0.2 0.7 ± 0.3	7.8 ± 0.3 7.5 ± 0.6	0.352 ± 0.008 0.173 ± 0.009	65.46 ± 3.32^1 30.99 ± 3.46^2
P3e	703.109429	25.5	42	0.778	-6.8 ± 0.3	11.1 ± 1.0	0.429 ± 0.029	79.92 ± 8.57^1
Q6e	712.286	89.3	78	2.028	-7.0 ± 0.1 ...	9.7 ± 0.3 4.4 ± 0.6	0.750 ± 0.017 0.180 ± 0.019	34.76 ± 1.11^1 3.75 ± 0.63^1
Q7e	712.388056	119.1	90	2.028	-6.9 ± 0.1 ...	8.9 ± 0.2 3.4 ± 0.8	0.801 ± 0.011 0.081 ± 0.017	34.08 ± 0.71^1 1.29 ± 0.43^1
Q8e	712.504639	153.1	102	2.028	-7.0 ± 0.3 1.1 ± 0.5 ...	8.3 ± 0.3 7.7 ± 0.8 3.8 ± 1.1	0.772 ± 0.018 0.189 ± 0.017 0.097 ± 0.041	30.55 ± 1.60^1 6.97 ± 1.22^2 1.76 ± 1.18^1
Q9e	712.635726	191.4	114	2.028	-7.4 ± 0.1	12.4 ± 0.2	0.692 ± 0.010	41.06 ± 0.68^1
Q10e	712.781294	233.9	126	2.027	-7.0 ± 0.1 ...	8.5 ± 0.2 4.6 ± 0.6	0.673 ± 0.007 0.117 ± 0.009	27.23 ± 0.53^1 2.58 ± 0.37^1
Q11e	712.941315	280.7	138	2.027	-7.4 ± 0.1 2.7 ± 0.7 ...	8.1 ± 0.3 5.9 ± 1.8 3.2 ± 1.0	0.592 ± 0.011 0.140 ± 0.011 0.117 ± 0.049	23.04 ± 0.75^1 3.96 ± 1.23^2 1.78 ± 1.21^2
Q13e	713.304602	386.9	162	2.026	-7.3 ± 0.2 -0.1 ± 0.7	7.2 ± 0.3 7.6 ± 1.0	0.419 ± 0.015 0.134 ± 0.013	14.52 ± 0.99^1 4.87 ± 1.00^2
Q14e	713.5078	446.5	174	2.026	-7.8 ± 0.2 0.2 ± 0.7 ...	6.1 ± 0.3 8.0 ± 1.2 3.2 ± 0.8	0.309 ± 0.010 0.109 ± 0.007 0.086 ± 0.032	9.08 ± 0.65^1 4.18 ± 0.81^2 1.33 ± 0.79^2
R0e	714.935627	0.0	6	1.371	-6.7 ± 0.3 2.4 ± 0.8	9.7 ± 0.5 8.0 ± 1.4	0.438 ± 0.011 0.112 ± 0.014	10.12 ± 0.63^1 2.13 ± 0.57^2
R1e	717.89124	4.3	18	1.251	-7.2 ± 0.1 1.4 ± 0.2	8.5 ± 0.1 6.5 ± 0.4	0.700 ± 0.007 0.152 ± 0.007	28.23 ± 0.54^1 4.66 ± 0.40^2
R3e	723.800848	25.5	42	1.19	-7.2 ± 0.1 2.1 ± 0.3	9.4 ± 0.3 7.6 ± 0.7	0.779 ± 0.019 0.212 ± 0.018	48.37 ± 2.25^1 10.63 ± 1.85^2
R4e	726.7547	42.5	54	1.184	-7.3 ± 0.1 1.1 ± 0.6	8.7 ± 0.2 7.5 ± 1.1	0.780 ± 0.013 0.154 ± 0.014	47.97 ± 1.81^1 8.20 ± 1.69^2
R5e	729.70782	63.8	66	1.183	-7.3 ± 0.1	11.6 ± 0.2	0.755 ± 0.013	65.02 ± 1.25^1
R6e	732.660136	89.3	78	1.187	-7.2 ± 0.2 -1.0 ± 1.4 ...	6.7 ± 0.8 11.0 ± 1.6 3.5 ± 0.7	0.698 ± 0.091 0.272 ± 0.042 0.183 ± 0.073	35.76 ± 8.44^1 22.99 ± 6.66^2 4.97 ± 2.84^1
R7e	735.611573	119.1	90	1.194	-7.5 ± 0.2 0.9 ± 0.7	8.3 ± 0.2 8.9 ± 0.9	0.760 ± 0.018 0.183 ± 0.014	49.65 ± 2.16^1 12.83 ± 2.13^2
R10e	744.459871	233.9	126	1.221	-7.9 ± 0.2 0.5 ± 0.6	8.1 ± 0.4 7.9 ± 0.9	0.574 ± 0.017 0.208 ± 0.017	38.59 ± 2.37^1 13.56 ± 2.32^2
R11e	747.407049	280.7	138	1.231	-7.3 ± 0.3 1.4 ± 0.7	9.9 ± 0.5 7.9 ± 1.1	0.468 ± 0.013 0.138 ± 0.021	38.86 ± 2.47^1 9.12 ± 2.33^2
R12e	750.352972	331.7	150	1.242	-7.5 ± 0.1	7.9 ± 0.3	0.420 ± 0.015	28.00 ± 1.26^1
R13e	753.297564	386.9	162	1.254	-7.9 ± 0.3 -0.5 ± 1.6	6.0 ± 0.7 12.0 ± 3.0	0.247 ± 0.046 0.139 ± 0.015	12.54 ± 3.54^1 14.14 ± 4.73^2
R15e	759.182446	510.2	186	1.278	-7.3 ± 0.6 1.3 ± 0.8	7.6 ± 1.0 8.4 ± 1.4	0.143 ± 0.011 0.108 ± 0.009	9.31 ± 1.58^1 7.76 ± 1.62^2
R17e	765.061068	650.4	210	1.302	-1.4 ± 0.7	15.4 ± 2.5	0.051 ± 0.006	6.77 ± 1.40^0
R18e	767.997835	726.9	222	1.315	-0.7 ± 0.5	7.9 ± 1.9	0.068 ± 0.012	4.70 ± 1.57^0

Note. See Table 2 for column descriptions. Data in the first five columns are from the HITRAN database (Gordon et al. 2017). Superscripts in the final column refer to which velocity component N_l will be totaled toward for the rotation diagrams in Section 3.4: ⁰none, ¹primary, ²secondary. Velocity for lines with more than one Gaussian is taken to be the that of the line with the largest τ_0 and the other Gaussian is recorded without velocity and in italics.

where N is the total column density, Q_R is the rotational partition function, E_l is the energy level of the lower state, and T_{ex} is the excitation temperature. We calculated Q_R for HCN and H^{13}CN for a given T_{ex} with the HITRAN python interface HAPI (Kochanov et al. 2016) and for HNC from levels published in ExoMol (Harris et al. 2006; Barber et al. 2013).

Figure 4 gives the rotation diagrams for HNC, H^{13}CN , and the two velocity components of HCN. This shows the linear relationship between $\ln(N_l/g_l)$ and E_l/k_B , implying that the LTE approximation holds. By linearly fitting to Equation (6), we obtain the values of T_{ex} and N for these species and

components, summarized in Table 5 along with their abundance relative to H_2 .

Several observations give $N_{\text{H}_2} \sim 10^{23}$ to $5 \times 10^{24} \text{cm}^{-2}$ toward IRc2 (e.g., Evans et al. 1991; Schilke et al. 1992; Sutton et al. 1995; Persson et al. 2007; Tercero et al. 2010; Favre et al. 2011; Plume et al. 2012; Crockett et al. 2014; Feng et al. 2015) and we adopt the most recent calculation derived from ALMA dust continuum emission, $N_{\text{H}_2} = (4.7 \pm 0.2) \times 10^{24} \text{cm}^{-2}$ (Peng et al. 2019), as it has a comparable beam size to SOFIA/EXES. However, uncertainties stand with adopting this value because the H_2 distribution may differ from the that of the

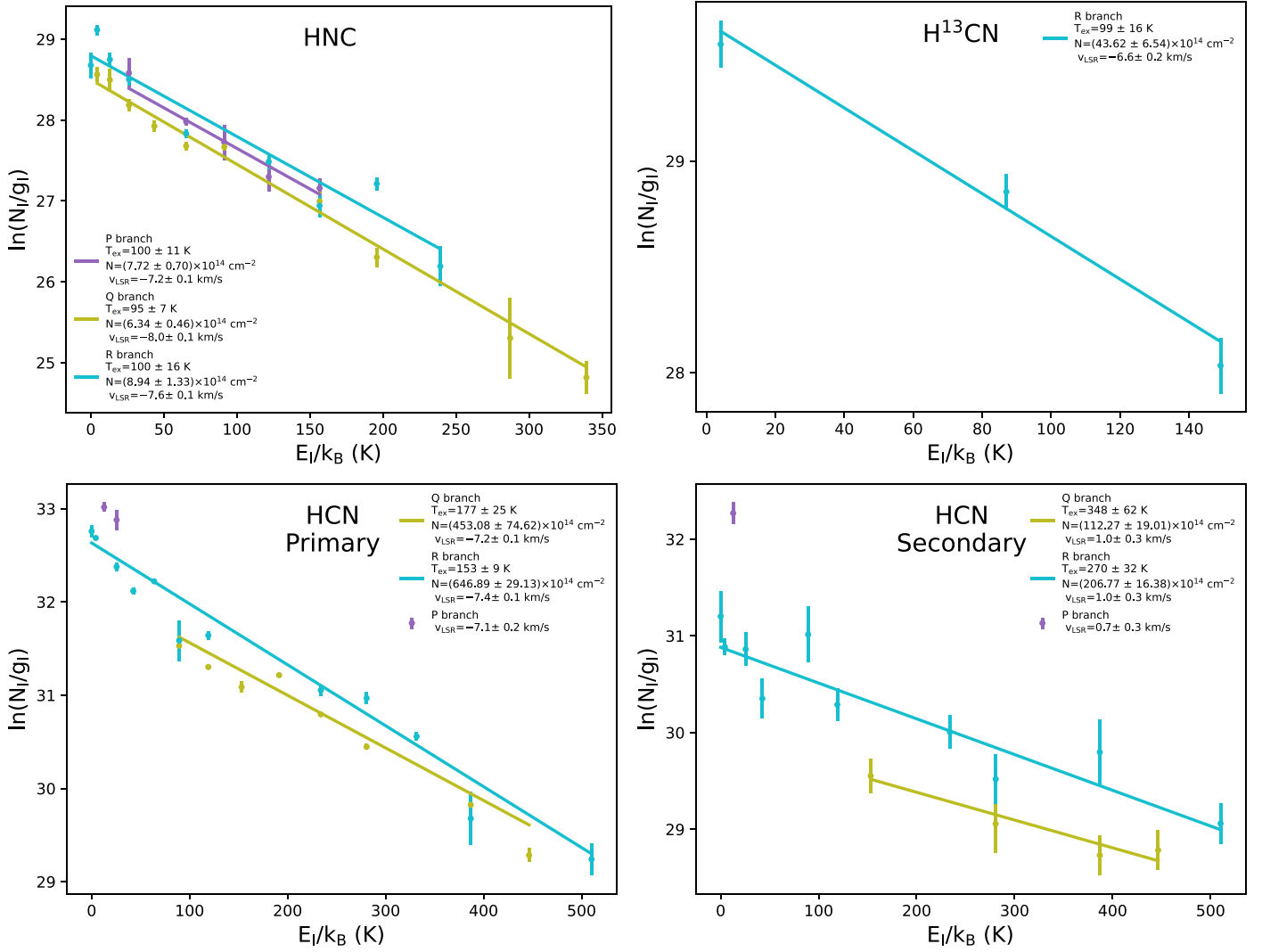


Figure 4. Rotation diagrams for HNC (top left), H¹³CN (top right), HCN primary velocity component (bottom left), and HCN secondary velocity component (bottom right). These follow Equation (6) where the excitation temperature and total column density of each species is extracted from the relation between the energy levels, column densities, and lower statistical weights of the transitions. The average local standard of rest velocity for each branch is also given.

larger molecules HCN and HNC, and these observations may correspond to a different component of the ISM toward IRC2. We do not fit the P branch of HCN, given only two points for the primary component and one for the secondary. Most of the P branch lines fall between observed settings.

Both HNC and H¹³CN trace the coldest gas at ~ 100 K, while HNC has a lower column density at $7.7 \times 10^{14} \text{ cm}^{-2}$ compared to $4.4 \times 10^{15} \text{ cm}^{-2}$ for H¹³CN. HCN traces the hottest, highest column density gas. Its primary velocity component (Q: 177 K; R: 153 K) is cooler than its secondary component (Q: 348 K; R: 270 K). However, the primary component has a higher column density (Q: $4.5 \times 10^{16} \text{ cm}^{-2}$; R: $6.5 \times 10^{16} \text{ cm}^{-2}$) compared to the secondary in both branches (Q: $1.1 \times 10^{16} \text{ cm}^{-2}$; R: $2.1 \times 10^{16} \text{ cm}^{-2}$).

4. Discussion

4.1. Interpretation of Results

The -7 km s^{-1} component of HNC, HCN, and H¹³CN has also been observed in the MIR by Rangwala et al. (2018) and Lacy et al. (2005) for HCN and C₂H₂, blueshifted with respect to the ambient cloud velocity of 9 km s^{-1} (Zapata et al. 2012).

As discussed in Rangwala et al. (2018), this velocity is similar to the northeast segment of the bipolar outflow originating from radio source I, which has been identified and mapped with SiO and H₂O masers (Genzel et al. 1981; Wright et al. 1995; Plambeck et al. 2009). Our -7 km s^{-1} lines may be associated with this outflow, being expelled material irradiated by IRC2, while the 1 km s^{-1} , hotter component is very likely closer to the hot core itself. Though we only resolved the 1 km s^{-1} component for HCN, the FWHMs of HNC in Table 2 are systematically larger than the HCN lines in Table 4. It may be that HNC also has a 1 km s^{-1} component that is unresolved. Our H¹³CN lines are too weak for comment.

The HNC column densities in Table 5 are consistently lower than HCN by about two orders of magnitude, evidence for a highly irradiated environment. Indeed, studies of planetary nebulae and the Helix Nebula find that HCN/HNC correlates with increasing UV radiation (Bublitz et al. 2019, 2020). HNC is less photostable than HCN (Chenel et al. 2016; Aguado et al. 2017) and is destroyed in increasingly advanced and hotter stages of stellar evolution (Jin et al. 2015). We see that toward Orion IRC2, HCN is more abundant and hotter compared to HNC, in support of these findings.

Table 5
Overview of Species Properties

Branch	v_{LSR} (km s ⁻¹)	T_{ex} (K)	N $\times 10^{14}$ cm ⁻²	N/N_{H_2} $\times 10^{-9}$
HNC				
P	-7.2 ± 0.1	100 ± 11	7.72 ± 0.70	0.16 ± 0.02
Q	-8.0 ± 0.1	95 ± 7	6.34 ± 0.46	0.13 ± 0.01
R	-7.6 ± 0.1	100 ± 16	8.94 ± 1.33	0.19 ± 0.03
HCN				
P	-7.1 ± 0.2 0.7 ± 0.3
Q	-7.2 ± 0.1 1.0 ± 0.3	177 ± 25 348 ± 62	453.08 ± 74.62 112.27 ± 19.01	9.64 ± 1.64 2.39 ± 0.42
R	-7.4 ± 0.1 1.0 ± 0.3	153 ± 9 270 ± 32	646.89 ± 29.13 206.77 ± 16.38	13.76 ± 0.85 4.40 ± 0.40
H ¹³ CN				
R	-6.6 ± 0.2	99 ± 16	43.62 ± 6.54	0.93 ± 0.14

Note. For each species, branch, and velocity component, v_{LSR} is the average LSR velocity, T_{ex} is the excitation temperature, N is the total column density, and N_{H_2} is the column density of H₂, adopted to be $4.7 \pm 0.2 \times 10^{24}$ cm⁻² (Peng et al. 2019). The HCN P branch did not have enough points for a linear fit to find temperature and column density.

A similar high-resolution ($\sim 55,000$ to $85,000$) MIR spectral survey covered the hot cores AFGL 2591 and AFGL 2136 from 4 to 13 μm with SOFIA/EXES, and the TEXES and the iSHELL instruments on the NASA Infrared Telescope Facility (Barr et al. 2020). In both hot cores, they identified transitions from the HCN ν_2 band, R branch that are also present in our Orion IRc2 survey. Their rotation diagrams for HCN yield temperatures 674.8 ± 32.0 K and 624.6 ± 19 K for AFGL 2591 and AFGL 2136 respectively. This is much hotter than the R-branch temperatures for IRc2 that we find, 153 ± 9 K and 270 ± 32 K for each velocity component. IRc2 may be cooler than these two conventional hot cores due to its lack of an internal heat source. Similar to our conclusion, Barr et al. (2020) find that the MIR probes hot gas at the center of hot cores, compared to the sub-millimeter which probes the outer envelope. Two previous studies also show that SOFIA/EXES detects molecules previously unobserved at longer wavelengths (Barr et al. 2018; Dungee et al. 2018).

4.2. Comparison to Previous IRc2 Observations

Table 6 summarizes derived velocities, temperatures, and column densities for HNC, HCN, and H¹³CN for observations toward Orion IRc2 from the literature and compares these to the present study. We take the average across all branches from Table 5 for each component to display in Table 6. The most apparent difference is that the two spectral regimes reveal different components toward Orion IRc2. The sub-millimeter/millimeter observations detect these three species in emission with a positive v_{LSR} while the MIR observations detect them in absorption with a negative v_{LSR} . Another difference is that all observations in the sub-millimeter/millimeter and MIR with ISO (Boonman et al. 2003) have a much larger beam size than EXES (Rangwala et al. 2018) and TEXES (Lacy et al. 2002, 2005). The smaller beam is important to observing the ISM component closest to the hot core. However, previous

MIR observations do not resolve the secondary HCN velocity component present in our work (Lacy et al. 2005; Rangwala et al. 2018). Our MIR observations are able to probe closer to the host core itself, and find the hottest measured temperature for HCN toward Orion IRc2 to date.

Table 7 compares HCN/HNC and ¹²C/¹³C ratios from this work to the literature. We use the average values over all branches of HCN, HNC, and H¹³CN from Table 1 for these ratios, taking only the -7 km s⁻¹ component of HCN, to find HCN/HNC = 72 ± 7 and ¹²C/¹³C = 13 ± 2 .

Our ratio HCN/HNC = 72 ± 7 falls within the the lower end of previous measurements that range from 75 to 300 (Goldsmith et al. 1986; Schilke et al. 1992; Comito et al. 2005). Such a range of values makes it difficult to draw direct a comparison between observations. Widely differing beam sizes may be responsible, where ours is the smallest at $3''/2$, and others are: $11''$ (Comito et al. 2005), $13''$ – $26''$ (Schilke et al. 1992), and $42''$ – $60''$ (Goldsmith et al. 1986). We should also note that we measure a different velocity components than the sub-millimeter/millimeter studies, and that there are no previous studies in the MIR with which to compare our results directly. Our smaller beam size allows us to probe the hot core more closely.

The ¹²C/¹³C = 13 ± 2 ratio toward IRc2 has been measured by more studies. Because we only saw three lines of H¹³CN, the uncertainty in the ratio may be larger than quoted. With SOFIA/EXES MIR measurements of C₂H₂, Rangwala et al. (2018) find ¹²C/¹³C = 14 ± 1 , similar to our value despite the difference in species to obtain it. Both these values are close to the Tercero et al. (2010) estimation for the hot core using H₂CS, 20 ± 9 , but are much lower than other measurements that range from 53 to 82.6 (Schilke et al. 1997; Favre et al. 2014; Feng et al. 2015), using HCN, HCOOCH₃, and CH₃CN respectively. Previous studies toward star-forming regions have found, however, that ¹²C/¹³C can differ depending on species, even isotopologues, due to differing formation pathways (Furuya et al. 2011; Yoshida et al. 2015; Taniguchi et al. 2016, 2017, 2019).

Our beam size is similar to one study at longer wavelengths (Feng et al. 2015), which derived the ratio using CH₃CN, and so differing beam sizes is not a likely explanation. The formation pathways for CH₃CN and HCN are also similar. Therefore, we consider a likely explanation for the lower ratio that we and Rangwala et al. (2018) find toward the hot core is that previous studies conducted in the sub-millimeter/millimeter and radio wavelengths observe different components of the ISM toward IRc2 than we do in the MIR.

With Orion’s distance from the Galactic center and a linear relation derived from Milam et al. (2005), Favre et al. (2014) calculated that the expected ratio is 50–90. This value is similar to measurements toward the neighboring compact ridge from 30 to 80 (Blake et al. 1987; Persson et al. 2007; Tercero et al. 2010; Gong et al. 2015).

If our HCN lines were to be optically thick, this may explain the low ratio. However, our lines lack the flat-bottomed profiles of optically thick lines. Our lines also display a sequence of depths with no sign of saturation, falling from 3% to 60% below the continuum level.

Our ¹²C/¹³C is comparable to the ratio toward the Galactic central hot core Sgr B2, ~ 20 (Favre et al. 2014; Giesen et al. 2020), which is expected for that region (Milam et al. 2005; Yan et al. 2019). Several measurements have found the ratio to

Table 6
Comparison of HNC, HCN, and H¹³CN Observations Toward Orion IRc2 between This and Previously Published Works

Reference	Region	Beam Size	τ	Type	v_{LSR} (km s ⁻¹)	T (K)	N ($\times 10^{14}$ cm ⁻²)
HNC							
This work	MIR	3''2	thin	abs	-7.6 \pm 0.1	98 \pm 7	7.67 \pm 0.52
Persson et al. (2007)	sub-mm	2''1	thin	emi	9	...	4.4
Comito et al. (2005)	sub-mm	11''	thin	emi	8	150 ^a	5
HCN							
This work	MIR	3''2	thin	abs	-7.3 \pm 0.1 1.0 \pm 0.2	165 \pm 13 309 \pm 35	549.99 \pm 40.05 159.52 \pm 12.55
Rangwala et al. (2018)	MIR	3''2	thin	abs	-5.2 \pm 2.8	140 \pm 10 ^b	840 \pm 60
Comito et al. (2005)	sub-mm	11''	thin	emi	5	150 ^a	700
Lacy et al. (2005)	MIR	1''5 ^c	...	abs	-10 ^d	150 ^d	...
Boonman et al. (2003)	MIR	14''	thick	abs	...	275 ^e	450
Schilke et al. (2001)	sub-mm	12''	thin	emi	...	100 ^f	260
Stutzki et al. (1988)	sub-mm	32''	thick	emi	6
Blake et al. (1987)	mm	30''	thick	emi	5.8	...	250
H ¹³ CN							
This work	MIR	3''2	thin	abs	-6.6 \pm 0.2	97 \pm 13	42.08 \pm 5.67
Schilke et al. (1992)	mm	26''	thin	emi	9.2 ^g	70 ^g	0.57

Notes. Left to right, columns refer to observation reference, spectral region, beam size, whether the observation is optically thin or thick, whether the line type is emission (emi) or absorption (abs), LSR velocity, temperature, and column density. Temperatures are calculated by a variety of methods, as detailed in table footnotes. The HNC and HCN values in this work are the averages across all branches for each component from Table 5. For reference, the ambient cloud velocity is 9 km s⁻¹ (Zapata et al. 2012).

^a Rotation temperature derived from DCN.

^b Excitation temperature, R branch only.

^c Beam size from Lacy et al. (2002), opacity unknown.

^d v_{LSR} and temperature approximation from HCN and C₂H₂ lines.

^e Modeled excitation temperature.

^f Rotation temperature derived from H¹⁵CN.

^g v_{LSR} and kinetic temperature estimated for entire hot core.

Table 7
Comparison of Observed Ratios Toward Orion IRc2

Reference	Region	Beam Size	Ratio
HCN/HNC			
This work	MIR	3''2	72 \pm 7
Comito et al. (2005)	sub-mm	11''	140
Schilke et al. (1992)	mm	26''	80 \pm 5
Goldsmith et al. (1986)	mm	42'', 60''	~200-300
¹² C/ ¹³ C			
This work	MIR	3''2	13 \pm 2 ^a
Rangwala et al. (2018)	MIR	3''2	14 \pm 1 ^b
Feng et al. (2015)	sub-mm	2''57	79.6 \pm 3.0 ^c
Favre et al. (2014)	mm	22''	\geq 53 ^d
Tercero et al. (2010)	mm	9''-29''	20 \pm 9 ^e
Schilke et al. (1997)	radio	20''	60 ^a

Notes. Species used to obtain ¹²C/¹³C ratio.

^a HCN.

^b C₂H₂.

^c CH₃CN.

^d HCOOCH₃.

^e H₂CS.

be lower in star-forming regions than in the local ISM: 20–50 (Daniel et al. 2013), \sim 30 toward a protostellar binary (Jørgensen et al. 2018), 45 \pm 3, (Magalhães et al. 2018), and

\sim 16 (Bøgelund et al. 2019) for various molecules. Colzi et al. (2020) suggest that an exchange reaction between ¹³C and C₃ can lead to a ¹³C enhancement in molecular clouds while they are still <30 K. This is cooler than our excitation temperatures for all species in Table 1. In this case, our low ratio may reflect conditions prior to protostellar warmup.

4.3. Comparison to a Hot Core Model

To compare our observations to modeling, we utilized the gas-grain chemical network as described in Acharyya & Herbst (2018) for the model in Figures 5 and 6. Both the gas-phase and grain-surface chemistry are treated via a rate equation approach. The major features of the model are as follows.

1. Model runs have two physical evolutionary phases as prescribed by Brown et al. (1988). In the first phase, freefall collapse (Figure 5), the cloud undergoes isothermal collapse at 10 K, from a density of 3000 to 10⁷ cm⁻³ in just under 10⁶ yr. During this period the visual extinction grows from 1.64 to 432 mag. In the second phase, warmup (Figure 6, left column), the collapse stops and the temperature increases linearly at the rate of 1 K/250 yr, which is a representative heating rate for high-mass star formation. We ran warmup models for five different final temperatures: 100, 150, 200, 270, and 300 K. Once the hot core reaches its final temperature, its

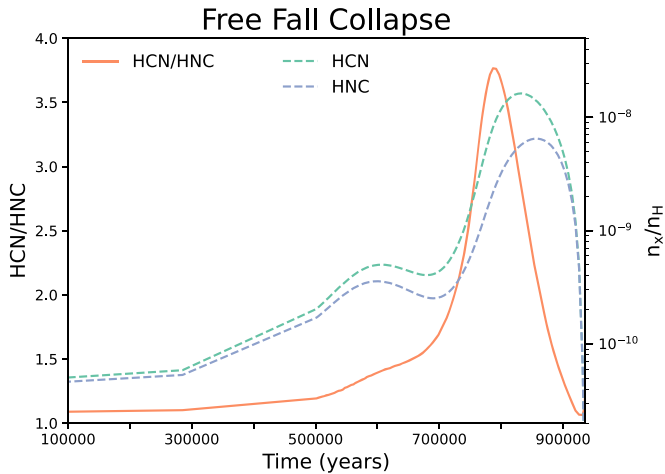


Figure 5. Time variation of HCN/HNC (orange solid line, left axis) and HCN and HNC abundances (green and blue dotted lines, right axis) during the freefall collapse phase of the model.

chemical evolution continues through the third phase, post-warmup, until 10^7 yr elapse (Figure 6, right column).

2. Graninger et al. (2014) found that the reaction $\text{HNC} + \text{H} \rightarrow \text{HCN} + \text{H}$ regulates the HCN/HNC ratio under all conditions. However, the activation barrier of this reaction is highly uncertain, and can vary between 0 and 2000 K. Therefore, we study the cases with and without the 2000 K activation barrier.
3. Classical dust grains are $0.1 \mu\text{m}$ in size with a surface site density $n_s = 1.5 \times 10^{15} \text{ cm}^{-2}$, leading to about 10^6 adsorption binding sites per grain.
4. We use standard low-metal elemental abundances, initially in the form of gaseous atoms with the exception of H_2 . Elements with ionization potentials below 13.6 eV take the form of singly charged positive ions (C^+ , Fe^+ , Na^+ , Mg^+ , S^+ , Si^+ , and Cl^+).
5. We use a sticking coefficient of 1, standard cosmic-ray ionization rate of 10^{-17} s^{-1} , and a diffusion-to-binding energy ratio of 0.5.

Figure 5 shows the time variation of HCN and HNC abundances during the freefall collapse phase during which the temperature is constant at 10 K. The peak abundances (relative to total atomic hydrogen) for HCN and HNC are 1.6×10^{-8} and 6.5×10^{-8} respectively. Toward the end of the first phase, HCN and HNC freeze out on the dust grains. The peak HCN/HNC ratio is ~ 3.8 .

Figure 6 shows the time variation of HCN and HNC for 10 different models during the warmup and post-warmup phases, with five different maximum temperatures of 100, 150, 200, 270, and 330 K, with or without the activation barrier. The left column of Figure 6 shows this chemical evolution during the warmup phase and the right column shows this in the post-warmup phase. Usually, the warmup phase lasts only up to $\sim 10^4$ yr. However, we have plotted up to 10^7 yr to show the effect of a long lifetime.

It is clear that for HCN the abundances for all models are very similar until the warmup phase, with the exception of the 100 K model. However in the post-warmup phase, models deviate slightly depending on activation barrier, and varying temperature causes more deviation. For HNC, the deviation with and without the activation barrier begins in the warmup phase by a factor of 20, and all 10 models deviate the most

during the post-warmup phase. Overall, the differences between models during the warmup phase are small, and they vary more during the post-warmup phase.

During post-warmup, the abundances for HCN in the 100 and 150 K models decrease by several orders of magnitude, whereas for the 200 K model the reduction is about two orders of magnitude, and for the 270 and 330 K models the change is minor. For HNC, a large reduction is present for all the models with no activation barrier. With a barrier, only the 100 and 150 K models show a large reduction.

Figure 6 also includes lines for $N_{\text{HCN}}/N_{\text{H}_2}$, $N_{\text{HNC}}/N_{\text{H}_2}$, and $N_{\text{HCN}}/N_{\text{HNC}}$ as measured from Table 5 taking the average across all branches for the -7 km s^{-1} velocity component. We do not display the 1 km s^{-1} component of HCN given that there is no similar component in HNC. Our observed values for N_x/N_{H_2} are comparable to the simulation's n_x/n_{H} because in this situation we can assume that all hydrogen is molecular. We take $N_{\text{H}_2} = (4.7 \pm 0.2) \times 10^{24} \text{ cm}^{-2}$ (Peng et al. 2019) as our default value from the literature, given the similarity in the ALMA beam size to EXES. However, as discussed in Section 3.4, the observed N_{H_2} toward IRC2 varies greatly. We also take the extreme values from $2 \times 10^{22} \text{ cm}^{-2}$ (Persson et al. 2007) to $5.4 \times 10^{24} \text{ cm}^{-2}$ (Favre et al. 2011). This shows how much the uncertainty in our HCN and HNC column densities is dwarfed by the range of values that N_{H_2} takes in the literature. Because of this, $N_{\text{HCN}}/N_{\text{HNC}}$ offers a much more robust comparison to the model.

Indeed, our HCN and HNC abundances fall short of all 10 models employed during the warmup phase. They coincide slightly for the 100 K no-barrier model at 2×10^6 yr, as well as the 150 K barrier model at about 7×10^6 yr. If we take into consideration, however, that our abundances are dependent on the widely varying N_{H_2} , then it is impossible to match our data to any one model as they all fall within the uncertainties. We prefer instead to make our prediction based on HCN/HNC, which does not require the molecular hydrogen column density. In this situation, our observations match the 150–330 K no-barrier models at about 10^6 yr. This is similar to the hot core age Rangwala et al. (2018) derived by matching their observed C_2H_2 and HCN abundances to hot core models.

The OMC-1 region was the site of a powerful explosion about 500 yr ago (Gómez et al. 2008). The 10^6 yr required to produce $\text{HCN}/\text{HNC} = 72 \pm 7$ is much longer than the 500 yr old explosive event in the Orion Molecular Cloud. Given the lack of evidence for an embedded protostar that internally heats IRC2, there are two explanations for this mismatch in timescales. The first is that IRC2 may have been irradiated prior to the explosive event by proximity to radio source I and was later expelled. As such, it would have resembled a traditional, internally heated hot core prior to explosion.

The second possible explanation is that our modeling does not take shock physics into account, and the inclusion of such may alter the timescales needed to reach our HCN/HNC ratio and our predicted age. Recent observations (Wright & Plambeck 2017) suggest the region is indeed shocked. The competing role of C-type shocks in the Galactic central hot core Sgr B2(N) has just been studied by Zhang et al. (2020). In addition, Willis et al. (2020) report new hot core models of Sgr B2(N) that use a single phase in which density and temperature are varied simultaneously in a study of isocyanides and cyanides, including HNC and HCN.

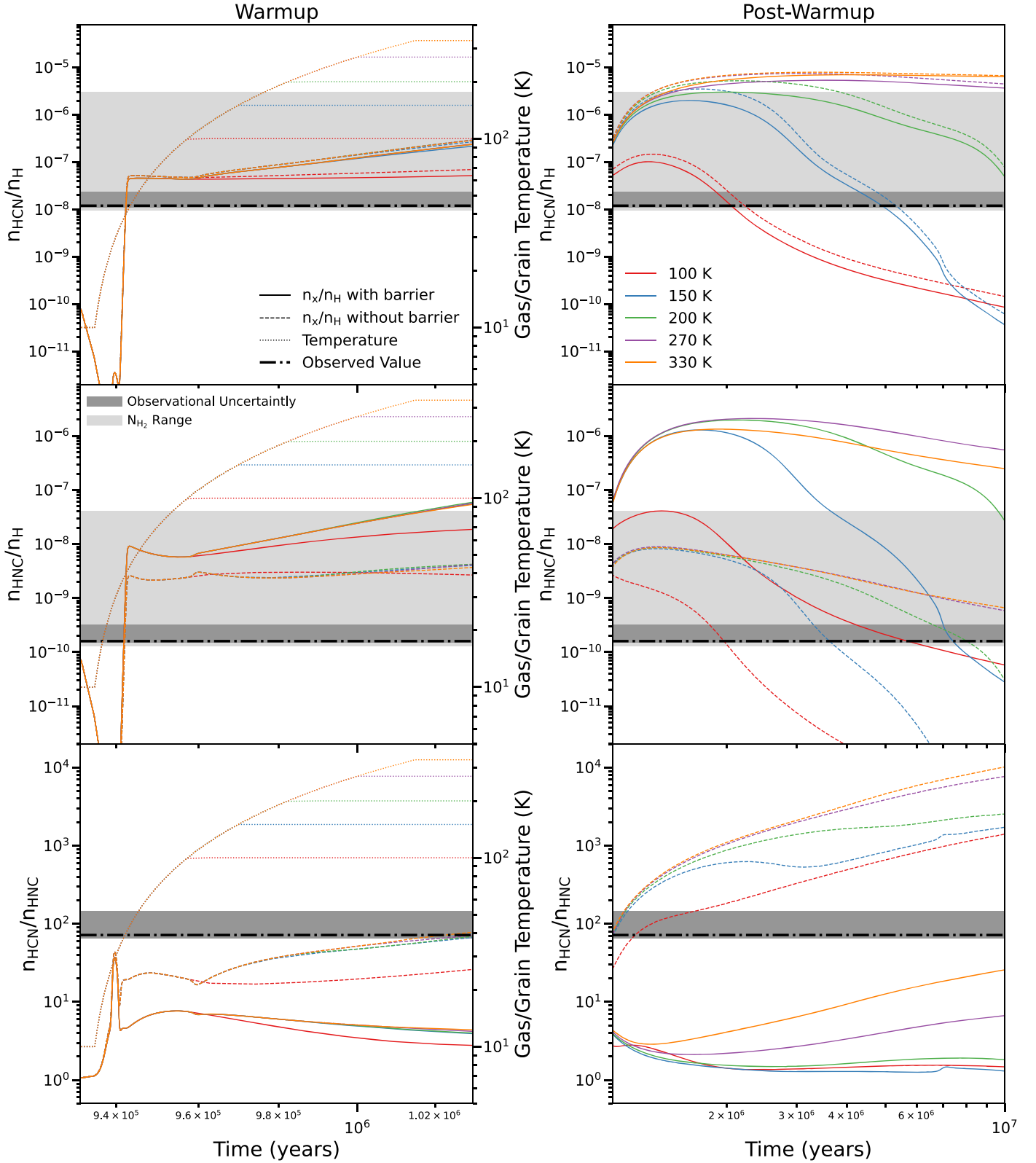


Figure 6. Time variation of HCN (top row), HNC (middle row), and HCN/HNC (bottom row) during the warmup (left column) and post-warmup phase (right column) on the left y-axes. Solid lines and dashed lines correspond to $\text{HNC} + \text{H} \rightarrow \text{HCN} + \text{H}$ with and without a 2000 K barrier respectively. Time variation of gas/grain temperature is shown by dotted lines corresponding to the right y-axis during the warmup phase. Colour for all three line types corresponds to the final temperature reached during the warmup phase. The horizontal dashed-dotted lines represent the observed values for $N_{\text{HCN}}/N_{\text{H}_2}$, $N_{\text{HNC}}/N_{\text{H}_2}$, and $N_{\text{HCN}}/N_{\text{HNC}}$ derived from Table 5 by taking the average across all branches for the -7 km s^{-1} component and using our adopted $N_{\text{H}_2} = (4.7 \pm 0.2) \times 10^{24} \text{ cm}^{-2}$ (Peng et al. 2019). The dark gray box corresponds to the error. The light gray box reflects the extrema in the measured N_{H_2} considering the lowest value $2 \times 10^{22} \text{ cm}^{-2}$ from Persson et al. (2007) and the highest value of $5.4 \times 10^{24} \text{ cm}^{-2}$ from Favre et al. (2011). Legends apply to all the panels.

5. Conclusions

From SOFIA/EXES we present high spectral resolution, MIR absorption spectra of HCN, HNC, and H^{13}CN toward the hot core Orion IRC2. These are the first MIR observations of HNC and H^{13}CN in the ISM. Almost continuous coverage of the P, Q, and R-branch transitions of HNC, and the Q and R-branch transitions of HCN, yield detailed rotation diagrams that produce the species' excitation temperatures and column densities. Only three H^{13}CN R-branch transitions are strong enough to include in a rotation diagram. All three species have an LSR velocity -7 km s^{-1} with average temperatures and column densities for HNC of 98 K and $7.7 \times 10^{14} \text{ cm}^{-2}$, H^{13}CN of 97 K and $4.2 \times 10^{15} \text{ cm}^{-2}$, and HCN of 165 K and $5.5 \times 10^{16} \text{ cm}^{-2}$. For the first time, we observe a second MIR velocity component of HCN measured at 1 km s^{-1} , 309 K, and $1.6 \times 10^{16} \text{ cm}^{-2}$.

Our -7 km s^{-1} absorption lines belong to the same component measured in the MIR toward Orion IRC2 by Rangwala et al. (2018) and Lacy et al. (2005), which probes different material than the emission lines observed in the sub-millimeter/millimeter (Blake et al. 1987; Stutzki et al. 1988; Schilke et al. 1992, 2001; Comito et al. 2005; Persson et al. 2007). It is clear that the MIR is key to studying the ISM closest to the hot core compared to longer wavelength observations in the sub-millimeter/millimeter. This -7 km s^{-1} component is similar in velocity to a bipolar outflow originating from nearby radio source I, which has no IR component. Our HCN, HNC, and H^{13}CN are likely associated with this outflow.

The HCN in the 1 km s^{-1} component is much hotter and because of this, represents material closer to the hot core itself. EXES's small beam size compared to previous MIR and most ground-based sub-millimeter/millimeter instruments allows us to isolate the material at the hot core's center. While HNC only has one clear velocity component, its line widths are consistently wider than HCN, hinting that it may have two components, albeit unresolved. HNC would be more depleted in this second, hotter component, making its detection difficult. We would expect HCN/HNC to be even higher in this hotter component. The H^{13}CN lines do not have a high enough signal-to-noise to comment on the possibility of a second component.

We find $\text{HCN}/\text{HNC} = 72 \pm 7$ in range of sub-millimeter/millimeter observations toward Orion IRC2 (Goldsmith et al. 1986; Schilke et al. 1992). This supports findings that this ratio is enhanced in hot, irradiated environments. Our isotopic ratio $^{12}\text{C}/^{13}\text{C} = 13 \pm 2$ is lower than expected for Orion IRC2's galactocentric distance, though similar to measurements by Rangwala et al. (2018) in the MIR and Tercero et al. (2010) in the millimeter.









In order to determine the age of the hot core, we run the chemical network of Acharyya & Herbst (2018) for a hot core model with three phases: freefall collapse, warmup, and post-warmup. Comparisons with HCN and HNC abundances alone are highly uncertain given the range in observed N_{H_2} toward IRC2. Instead, we use our observed HCN/HNC ratio to find that the hot core is $\sim 10^6$ yr old. This supports similar results in Rangwala et al. (2018).

This work demonstrates the importance of the MIR in accessing transitions of HCN, HNC, and H^{13}CN that originate in hotter material closer to the hot core compared to commonly used rotational transitions in the sub-millimeter/millimeter. The spectra presented here are a part of a larger survey with SOFIA/EXES toward Orion IRC2. Future papers detailing

more molecular species are forthcoming. These studies will be critical in informing the observations from the James Webb Space Telescope (JWST) which, while more sensitive, lacks the resolving power of SOFIA/EXES. With SOFIA/EXES we can unambiguously identify the signals from the strongest molecular species and construct a reference database to inform the search for weaker molecular species in JWST spectra.

This work made use of the following Python packages: Astropy (Robitaille et al. 2013; Price-Whelan et al. 2018), Matplotlib (Hunter 2007), Numpy (van der Walt et al. 2011), Scipy (Virtanen et al. 2020), and HAPI (Kochanov et al. 2016). We would also like to thank James De Buizer for providing FORCAST data, Kyle Kaplan for the useful conversation, and the anonymous reviewer for their helpful suggestions. S.N. gratefully acknowledges funding from the BAERI cooperative agreement 80NSSC17M0014. T.J.L. and X.H. gratefully acknowledge financial support from the NASA 16-PDART16_2-0 080, 17-APRA17-0051, and 18-APRA18-0013 grants. X.H. acknowledges the NASA/SETI Cooperative Agreements NNX15AF45A, NNX17AL03G and 80NSSC19M0121. M.N.D. is supported by the Swiss National Science Foundation (SNSF) Ambizione grant 180079, the Center for Space and Habitability (CSH) Fellowship, and the IAU Gruber Foundation Fellowship. R.C.F. acknowledges funding from NASA grant NNX17AH15G.

ORCID iDs

Sarah Nickerson  <https://orcid.org/0000-0002-7489-3142>
 Naseem Rangwala  <https://orcid.org/0000-0001-9920-7391>
 Sean W. J. Colgan  <https://orcid.org/0000-0001-6275-7437>
 Curtis DeWitt  <https://orcid.org/0000-0002-6528-3836>
 Xinchuan Huang  <https://orcid.org/0000-0003-2458-5050>
 Kinsuk Acharyya  <https://orcid.org/0000-0002-0603-8777>
 Maria Drozdovskaya  <https://orcid.org/0000-0001-7479-4948>
 Ryan C. Fortenberry  <https://orcid.org/0000-0003-4716-8225>
 Eric Herbst  <https://orcid.org/0000-0002-4649-2536>
 Timothy J. Lee  <https://orcid.org/0000-0002-2598-2237>

References

- Aalto, S., Garcia-Burillo, S., Muller, S., et al. 2012, *A&A*, 537, A44
 Acharyya, K., & Herbst, E. 2018, *ApJ*, 859, 51
 Aguado, A., Roncero, O., Zanchet, A., Agúndez, M., & Cernicharo, J. 2017, *ApJ*, 838, 33
 Agúndez, M., Biver, N., Santos-Sanz, P., Bockelée-Morvan, D., & Moreno, R. 2014, *A&A*, 564, L2
 An, D., Ramírez, S. V., Sellgren, K., et al. 2009, *ApJ*, 702, 128
 An, D., Ramírez, S. V., Sellgren, K., et al. 2011, *ApJ*, 736, 133
 Bally, J., Ginsburg, A., Arce, H., et al. 2017, *ApJ*, 837, 60
 Barber, R. J., Strange, J. K., Hill, C., et al. 2013, *MNRAS*, 437, 1828
 Barr, A. G., Boogert, A., Dewitt, C. N., et al. 2018, *ApJL*, 868, L2
 Barr, A. G., Boogert, A., DeWitt, C. N., et al. 2020, *ApJ*, 900, 104
 Belloche, A., Müller, H. S., Menten, K. M., Schilke, P., & Comito, C. 2013, *A&A*, 559, A47
 Benson, P. J., & Myers, P. C. 1989, *ApJS*, 71, 89
 Bisschop, S. E., Jørgensen, J. K., van Dishoeck, E. F., & de Wachter, E. B. 2007, *A&A*, 465, 913
 Blake, G. A., Mundy, L. G., Carlstrom, J. E., et al. 1996, *ApJL*, 472, L49
 Blake, G. A., Sutton, E. C., Masson, C. R., & Phillips, T. G. 1987, *ApJ*, 315, 612
 Bøgelund, E. G., Barr, A. G., Taquet, V., et al. 2019, *A&A*, 628, A2
 Boonman, A. M., van Dishoeck, E. F., Lohuis, F., et al. 2003, *A&A*, 399, 1047

- Boonman, A. M. S., Stark, R., van der Tak, F. F. S., et al. 2001, *ApJL*, **553**, L63
- Bottinelli, S., Ceccarelli, C., Lefloch, B., et al. 2004, *ApJ*, **615**, 354
- Bowman, J. M., Gazdy, B., Bentley, J. A., Lee, T. J., & Dateo, C. E. 1993, *JChPh*, **99**, 308
- Brown, P. D., Charnley, S. B., & Millar, T. J. 1988, *MNRAS*, **231**, 409
- Bublitz, J., Kastner, J., Hily-Blant, P., et al. 2020, *Galax*, **8**, 32
- Bublitz, J., Kastner, J. H., Santander-García, M., et al. 2019, *A&A*, **625**, 1
- Bujarrabal, V., Fuente, A., & Omont, A. 1994, *A&A*, **285**, 247
- Cernicharo, J., Barlow, M. J., Gonzalez-Alfonso, E., et al. 1996, *A&A*, **204**, L201
- Cernicharo, J., Daniel, F., Castro-Carrizo, A., et al. 2013, *ApJL*, **778**, L25
- Cesaroni, R. 2005, in *IAU Symp. 227, Massive Star Birth: A Crossroads of Astrophysics*, ed. R. Cesaroni et al. (Cambridge: Cambridge Univ. Press), 59
- Chenel, A., Roncero, O., Aguado, A., Agúndez, M., & Cernicharo, J. 2016, *JChPh*, **144**, 144306
- Clarke, M., Vacca, W. D., & Shuping, R. Y. 2015, *adass*, **24**, 355
- Colzi, L., Fontani, F., Caselli, P., et al. 2018a, *A&A*, **609**, A129
- Colzi, L., Fontani, F., Rivilla, V. M., et al. 2018b, *MNRAS*, **478**, 3693
- Colzi, L., Sipilä, O., Roueff, E., Caselli, P., & Fontani, F. 2020, *A&A*, **640**, A51
- Comito, C., Schilke, P., Phillips, T. G., et al. 2005, *ApJS*, **156**, 127
- Crockett, N. R., Bergin, E. A., Neill, J. L., et al. 2014, *ApJ*, **787**, 112
- Daniel, F., Gérin, M., Roueff, E., et al. 2013, *A&A*, **560**, 1
- de Buizer, J. M., Morris, M. R., Becklin, E. E., et al. 2012, *ApJ*, **749**, 35
- de Graauw, T., Haser, L. N., Beintema, D. A., et al. 1996, *A&A*, **315**, L47
- Dungee, R., Boogert, A., Dewitt, C. N., et al. 2018, *ApJL*, **868**, L10
- Dutrey, A., Guilloteau, S., & Guélin, M. 1997, *A&A*, **317**, 55
- Evans, N. J., Lacy, J. H., & Carr, J. S. 1991, *ApJ*, **383**, 674
- Favre, C., Carvajal, M., Field, D., et al. 2014, *ApJS*, **215**, 25
- Favre, C., Despois, D., Brouillet, N., et al. 2011, *A&A*, **532**, A32
- Feng, S., Beuther, H., Henning, T., et al. 2015, *A&A*, **590**, C1
- Furuya, K., Aikawa, Y., Sakai, N., & Yamamoto, S. 2011, *ApJ*, **731**, 38
- Gao, Y., & Solomon, P. M. 2004, *ApJS*, **152**, 63
- Genzel, R., Reid, M. J., Moran, J. M., & Downes, D. 1981, *ApJ*, **244**, 884
- Giesen, T. F., Mookerjee, B., Fuchs, G. W., et al. 2020, *A&A*, **633**, A120
- Goddi, C., Greenhill, L. J., Humphreys, E. M., Chandler, C. J., & Matthews, L. D. 2011, *ApJL*, **739**, L13
- Goldsmith, P. F., Irvine, W. M., Hjalmarson, A., & Elder, J. 1986, *ApJ*, **310**, 383
- Goldsmith, P. F., & Langer, W. D. 1999, *ApJ*, **517**, 209
- Goldsmith, P. F., Langer, W. D., Elder, J., Irvine, W., & Kollberg, E. 1981, *ApJ*, **249**, 524
- Gómez, L., Rodríguez, L. F., Loinard, L., et al. 2008, *ApJ*, **685**, 333
- Gong, Y., Henkel, C., Thorwirth, S., et al. 2015, *A&A*, **581**, A48
- Gordon, I. E., Rothman, L. S., Hill, C., et al. 2017, *JQSRT*, **203**, 3
- Graninger, D., Öberg, K. I., Qi, C., & Kastner, J. 2015, *ApJL*, **807**, L15
- Graninger, D. M., Herbst, E., Öberg, K. I., & Vasyunin, A. I. 2014, *ApJ*, **787**, 74
- Guélin, M., Salomé, P., Neri, R., et al. 2007, *A&A*, **462**, L45
- Hacar, A., Bosman, A. D., & van Dishoeck, E. F. 2020, *A&A*, **635**, A4
- Harada, N., Riquelme, D., Viti, S., et al. 2015, *A&A*, **584**, A102
- Harris, A. I., Avery, L. W., Schuster, K.-F., Tacconi, L. J., & Genzel, R. 1995, *ApJL*, **446**, L85
- Harris, G. J., Pavlenko, Y. V., Jones, H. R., & Tennyson, J. 2003, *MNRAS*, **344**, 1107
- Harris, G. J., Tennyson, J., Kaminsky, B. M., Pavlenko, Y. V., & Jones, H. R. 2006, *MNRAS*, **367**, 400
- Henkel, C., Mauersberger, R., & Schilke, P. 1988, *A&A*, **201**, L23
- Herbst, E. 1978, *ApJ*, **222**, 508
- Hernández Vera, M., Lique, F., Dumouchel, F., Hily-Blant, P., & Faure, A. 2017, *MNRAS*, **468**, 1084
- Herpin, F., & Cernicharo, J. 2000, *ApJL*, **530**, L129
- Hirota, T., Kim, M. K., Kurono, Y., & Honma, M. 2015, *ApJ*, **801**, 82
- Hirota, T., Machida, M. N., Matsushita, Y., et al. 2017, *NatAs*, **1**, 0146
- Hirota, T., Yamamoto, S., Mikami, H., & Ohishi, M. 1998, *ApJ*, **503**, 717
- Ho, P. T. P., Barrett, A. H., Myers, P. C., et al. 1979, *ApJ*, **234**, 912
- Houck, J. R., Roellig, T. L., van Cleve, J., et al. 2004, *ApJ*, **154**, 18
- Hrivnak, B. J., Volk, K., & Kwok, S. 2000, *ApJ*, **535**, 275
- Hunter, J. D. 2007, *CSE*, **9**, 99
- Indriolo, N., Neufeld, D. A., Barr, A. G., et al. 2020, *ApJ*, **894**, 107
- Indriolo, N., Neufeld, D. A., DeWitt, C. N., et al. 2015a, *ApJL*, **802**, L14
- Indriolo, N., Neufeld, D. A., Gerin, M., et al. 2015b, *ApJ*, **800**, 40
- Irvine, W. M., & Schloerb, F. P. 1984, *ApJ*, **282**, 516
- Jacquinet-Husson, N., Armante, R., Scott, N. A., et al. 2016, *JMoSp*, **327**, 31
- Jin, M., Lee, J. E., & Kim, K. T. 2015, *ApJ*, **219**, 2
- Jørgensen, J. K., Müller, H. S., Calcutt, H., et al. 2018, *A&A*, **620**, A170
- Kastner, J. H., Zuckerman, B., Weintraub, D. A., & Forveille, T. 1997, *Sci*, **277**, 67
- Knez, C., Boonman, A. M. S., Lacy, J. H., Evans, N. J. I., & Richter, M. J. 2001, *AAS Meeting*, **199**, 134.10
- Knez, C., Lacy, J. H., Evans, N. J., van Dishoeck, E. F., & Richter, M. J. 2009, *ApJ*, **696**, 471
- Kochanov, R. V., Gordon, I. E., Rothman, L. S., et al. 2016, *JQSRT*, **177**, 15
- Kounkel, M., Hartmann, L., Loinard, L., et al. 2017, *ApJ*, **834**, 142
- Kurtz, S. E., Cesaroni, R., Churchwell, E. B., Hofner, P., & Walmsley, C. M. 2000, in *Protostars and Planets IV*, ed. V. Mannings et al. (Tucson, AZ: Univ. Arizona Press)
- Lacy, J. H., Knez, C., Evans, N. J., & Richter, M. J. 2005, *AAS Meeting*, **207**, 81.22
- Lacy, J. H., Richter, M. J., Greathouse, T. K., Jaffe, D. T., & Zhu, Q. 2002, *PASP*, **114**, 153
- Lahuis, F., & van Dishoeck, E. F. 2000, *A&A*, **355**, 699
- Lahuis, F., van Dishoeck, E. F., Boogert, A. C. A., et al. 2006, *ApJL*, **636**, L145
- Lee, T. J., & Rendell, A. P. 1991, *CPL*, **177**, 491
- Lis, D. C., Keene, J., Young, K., et al. 1997, *Icar*, **130**, 355
- Liszt, H., & Lucas, R. 2001, *A&A*, **370**, 576
- Lo, J. I., Chou, S. L., Peng, Y. C., et al. 2015, *ApJS*, **221**, 20
- Loison, J. C., Wakelam, V., & Hickson, K. M. 2014, *MNRAS*, **443**, 398
- Lord, S. D. 1992, NASA Technical Memorandum 103957, <https://atran.arc.nasa.gov/cgi-bin/atran/atran.cgi>
- Loughnane, R. M., Redman, M. P., Thompson, M. A., et al. 2012, *MNRAS*, **420**, 1367
- Magalhães, V. S., Hily-Blant, P., Faure, A., Hernandez-Vera, M., & Lique, F. 2018, *A&A*, **615**, 1
- McGuire, B. A. 2018, *ApJS*, **239**, 17
- Mendes, M. B., Buhr, H., Berg, M. H., et al. 2012, *ApJL*, **746**, L8
- Miettinen, O. 2014, *A&A*, **562**, A3
- Milam, S. N., Savage, C., Brewster, M. A., Ziurys, L. M., & Wyckoff, S. 2005, *ApJ*, **634**, 1126
- Moreno, R., Lellouch, E., Lara, L. M., et al. 2011, *A&A*, **536**, L12
- Nguyen, T. L., Baraban, J. H., Ruscic, B., & Stanton, J. F. 2015, *JPCA*, **119**, 10929
- Ohishi, M. 1997, in *IAU Symp. 178*, 61
- Okumura, S. I., Yamashita, T., Sako, S., et al. 2011, *PASJ*, **63**, 823
- Orozco-Aguilera, M. T., Zapata, L. A., Hirota, T., Qin, S.-L., & Masqué, J. M. 2017, *ApJ*, **847**, 66
- Peng, Y., Rivilla, V. M., Zhang, L., Ge, J. X., & Zhou, B. 2019, *ApJ*, **871**, 251
- Pérez-Beaupuits, J. P., Aalto, S., & Gerebro, H. 2007, *A&A*, **476**, 177
- Persson, C. M., Olofsson, A. O. H., Koning, N., et al. 2007, *A&A*, **476**, 807
- Plambeck, R. L., Wright, M. C., Friedel, D. N., et al. 2009, *ApJL*, **704**, L25
- Plambeck, R. L., & Wright, M. C. H. 2016, *ApJ*, **833**, 219
- Plume, R., Bergin, E. A., Phillips, T. G., et al. 2012, *ApJ*, **744**, 28
- Price-Whelan, A. M., Sipilä, B. M., Günther, H. M., et al. 2018, *AJ*, **156**, 123
- Rangwala, N., Colgan, S. W. J., le Gal, R., et al. 2018, *ApJ*, **856**, 9
- Richter, M. J., DeWitt, C. N., McKelvey, M., et al. 2018, *JAI*, **7**, 1840013
- Rickard, L. J., Palmer, P., Turner, B. E., Morris, M., & Zuckerman, B. 1977, *ApJ*, **214**, 390
- Rivilla, V. M., Beltrán, M. T., Cesaroni, R., et al. 2017, *A&A*, **598**, A59
- Robitaille, T. P., Tollerud, E. J., Greenfield, P., et al. 2013, *A&A*, **558**, A33
- Rolfes, R., Schilke, P., Wyrowski, F., et al. 2011, *A&A*, **529**, A76
- Sarrasin, E., ben Abdallah, D., Wernli, M., et al. 2010, *MNRAS*, **404**, 518
- Schilke, P., Benford, D. J., Hunter, T. R., Lis, D. C., & Phillips, T. G. 2001, *ApJS*, **132**, 281
- Schilke, P., Groesbeck, T. D., Blake, G. A., & Phillips, T. G. 1997, *ApJS*, **108**, 301
- Schilke, P., Walmsley, C. M., Pineau des Forêts, G., et al. 1992, *A&A*, **256**, 595
- Shuping, R. Y., Morris, M., & Bally, J. 2004, *AJ*, **128**, 363
- Snyder, L. E., & Buhl, D. 1971, *ANYAS*, **194**, 17
- Snyder, L. E., & Buhl, D. 1972, *ApJ*, **177**, 619
- Stutzki, J., Genzel, R., Harris, A. I., Herman, J., & Jaffe, D. T. 1988, *ApJL*, **330**, L125
- Sutton, E. C., Peng, R., Danchi, W. C., et al. 1995, *ApJS*, **97**, 455
- Taniguchi, K., Herbst, E., Ozeki, H., & Saito, M. 2019, *ApJ*, **884**, 167
- Taniguchi, K., Ozeki, H., & Saito, M. 2017, *ApJ*, **846**, 46
- Taniguchi, K., Saito, M., & Ozeki, H. 2016, *ApJ*, **830**, 106
- Tennekes, P. P., Harju, J., Juvela, M., & Tóth, L. V. 2006, *A&A*, **456**, 1037
- Tercero, B., Cernicharo, J., Pardo, J. R., & Goicoechea, J. R. 2010, *A&A*, **517**, A96

- Turner, B. E., Pirgov, L., & Minh, Y. C. 1997, [ApJ](#), **483**, 235
- van der Tak, F. F. 2004, in IAU Symp. 221, Star Formation at High Angular Resolution, ed. M. Burton et al. (San Francisco, CA: ASP), 59
- van der Walt, S., Colbert, S. C., & Varoquaux, G. 2011, [CSE](#), **13**, 22
- van Dishoeck, E. F., Wright, C. M., Helmich, F. P., et al. 1998, [ApJ](#), **502**, L173
- Vasyunina, T., Linz, H., Henning, T., et al. 2011, [A&A](#), **527**, A88
- Virtanen, P., Gommers, R., Oliphant, T. E., et al. 2020, [Nature Methods](#), **17**, 261
- Wampfler, S. F., Jørgensen, J. K., Bizzarro, M., & Bisschop, S. E. 2014, [A&A](#), **572**, A24
- Willis, E. R., Garrod, R. T., Belloche, A., et al. 2020, [A&A](#), **636**, A29
- Wright, M. C. H., & Plambeck, R. L. 2017, [ApJ](#), **843**, 83
- Wright, M. C. H., Plambeck, R. L., Mundy, L. G., & Looney, L. W. 1995, [ApJL](#), **455**, L185
- Yan, Y. T., Zhang, J. S., Henkel, C., et al. 2019, [ApJ](#), **877**, 154
- Yoshida, K., Sakai, N., Tokudome, T., et al. 2015, [ApJ](#), **807**, 66
- Young, E. T., Becklin, E. E., Marcum, P. M., et al. 2012, [ApJL](#), **749**, L17
- Zapata, L. A., Rodríguez, L. F., Schmid-Burgk, J., et al. 2012, [ApJL](#), **754**, L17
- Zapata, L. A., Schmid-Burgk, J., & Menten, K. M. 2011, [A&A](#), **529**, A24
- Zeng, S., Jiménez-Serra, I., Cosentino, G., et al. 2017, [A&A](#), **603**, A22
- Zhang, X., Quan, D., Chang, Q., et al. 2020, [MNRAS](#), **497**, 609
- Zuckerman, B., Morris, M., Palmer, P., & Turner, B. E. 1972, [ApJL](#), **173**, L125